ACS APPLIED MATERIALS & INTERFACES

www.acsami.org

Research Article

Dopamine Hydrochloride-Assisted Synergistic Modulation of Perovskite Crystallization and Sn^{2+} Oxidation for Efficient and Stable Lead-free Solar Cells

Wenbo Jia, Zijie Wei, Bingxu Liu, Dongdong Yan, Yunze Huang, Meicheng Li, Ye Tao, Runfeng Chen,* and Ligang Xu*

Cite This: *ACS Appl. Mater. Interfaces* 2022, 14, 46801−46808

Read Online

ACCESS | Metrics & More | Article Recommendations | Supporting Information

ABSTRACT: Tin perovskites have received great concern in solar cell research owing to their favorable optoelectronic performance and environmental friendliness. However, due to their poor crystallization and easy oxidation, the performance improvement for tin-based perovskite solar cells (TPSCs) is rather challenging. Herein, reductive 3-hydroxytyramine hydrochloride (DACl) with NH_2·HCl and phenol groups as co-additives with SnF_2 is added into the precursor to modulate perovskite crystallization and inhibit Sn^{2+} oxidation for high-performance TPSCs. The Lewis base group of NH_2 HCl in DACl could bind to perovskite lattices to modulate the crystallization with suppressed defects in the bulk and grain boundary, whereas reductive phenol groups effectively constrain the Sn^{2+} oxidation. Moreover, the undissociated DACl decreases the supersaturated concentration of tin perovskite solution and creates a pre-nucleation site for rapid nucleation to further regulate crystallization. Consequently, the DACl-derived TPSCs achieve a high power-conversion efficiency (PCE) that reaches up to 11%. More impressively, the device remains at 84% of the initial PCE after full-sun illumination in N_2 over 600 h without being encapsulated. This DACl-based synergistic modulation of a lead-free perovskite demonstrates a feasible approach using one molecule with different functional groups to manipulate crystallization, Sn^{2+} oxidation, and defect reparation of tin perovskite films, providing a critical guideline for constructing high-quality perovskites by multifunctional additives with high photovoltaic performance.

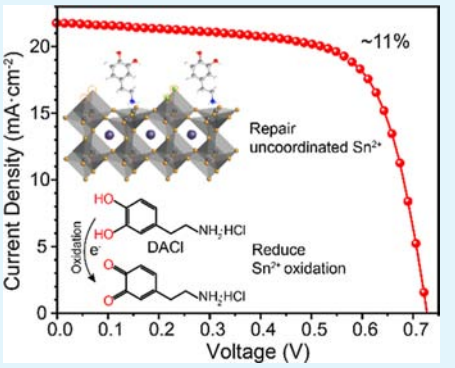

KEYWORDS: *lead-free perovskite solar cells, multifunctional additives, synergistic modulation, crystallization, power-conversion efficiency*

INTRODUCTION

Perovskite solar cells have attracted great concern owing to their fabulous electrical and optical properties with a certified efficiency of over 25%.[1] Nevertheless, the involvement of lead in traditional perovskite materials, which is a potential risk of biological toxicity to human health and an environmental hazard, hampers their future commercialization.[2−7] Therefore, various methods have been developed to construct lead-free photovoltaic devices by substituting lead with less or non-toxic elements, such as germanium (Ge), antimony (Sb), and tin (Sn).[8−12] Among them, Sn is the most promising candidate due to its suitable ionic radius[13] and electronic configuration (ns^2np^2).[14] Moreover, Sn perovskites exhibit excellent photoelectric properties, for example, suitable band gap (1.2−1.4 eV) approaching the Shockley−Queisser limit (1.34 eV),[15−17] low exciton-binding energy (18 meV), and high carrier mobility.[18−20] Nevertheless, tin-based perovskite solar cells (TPSCs) still show lower power-conversion efficiency (PCEs) and stability compared to lead-based devices, mainly due to the poor crystallization and easy oxidation of Sn^{2+}.[21]

Poor crystallization induces abundant defects and wrinkles in tin perovskites and promotes the infiltration of water and oxygen into the Sn perovskite film, thereby accelerating the degradation of TPSCs.[22] To address this issue, considerable efforts have been made to modulate Sn perovskite crystallization, including solvent engineering for the generated intermediate adduct (SnI_2-3DMSO)[23] and retarded crystal growth and additive engineering by employing ammonium thiocyanate (NH_4SCN) to control the crystallization process with a preferable orientation.[24] Our group also developed a vapor incubation method to fabricate high-quality perovskite films, leading to a PCE of over 10% along with enhanced device stability.[7] Since iodide (I^-) and alkylammonium (FA^+ and MA^+) ions are easy to volatilize in annealing and form

Received: June 28, 2022
Accepted: September 5, 2022
Published: October 10, 2022

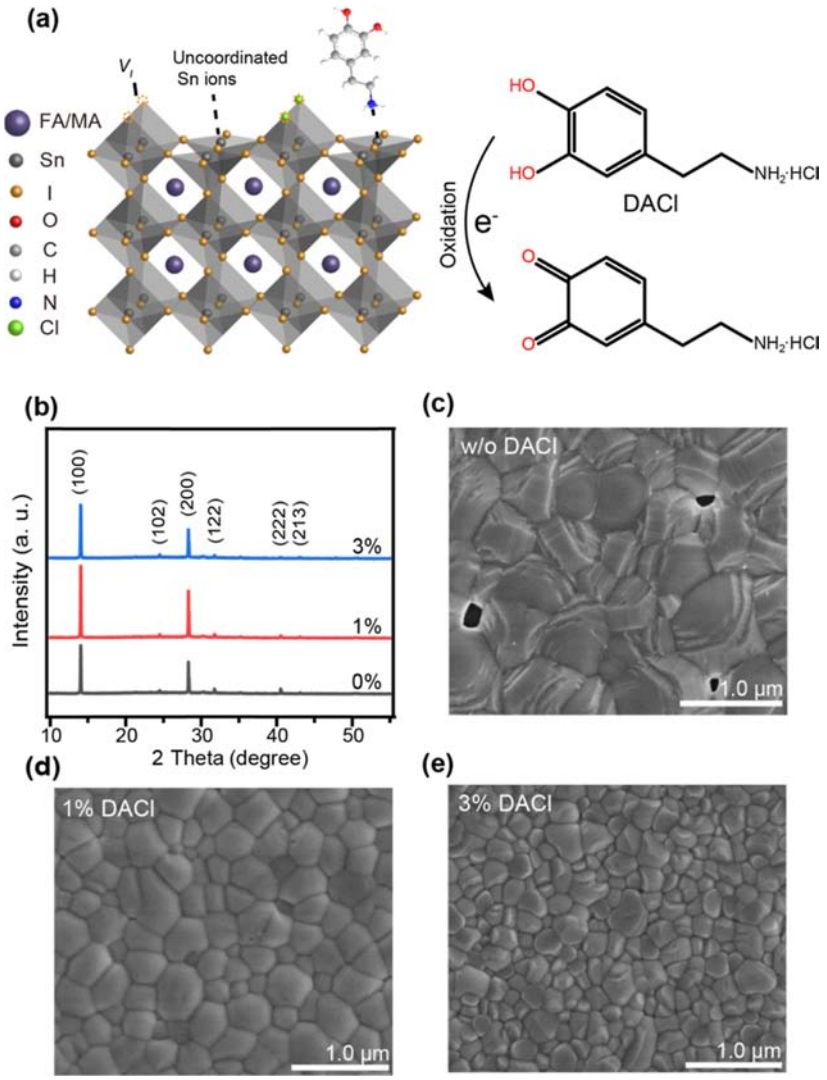

Figure 1. (a) Schematic illustration of the DACl-derived synergistic reparation of perovskite defects on the perovskite crystal lattice and chemical reaction when DACl is exposed to O_2. (b–e) XRD patterns (b) and top-view SEM images (c–e) of $FA_{0.75}MA_{0.25}SnI_3$ films with different doping molar contents of DACl.

vacancies, the fast nucleation process generates perovskite films with low vacancies and smooth morphology.[25−29] Thus, it is urgent to control the nucleation process for high-quality Sn perovskite films.

The easy oxidation of Sn^{2+} is another source of TPSCs' inferior photovoltaic performance attributed to serious self-p-doping, mismatch of energy alignment, and high defect density of states.[30] Therefore, it is crucial to inhibit the oxidation of Sn^{2+} in high-performance TPSCs. The introduction of Sn power, SnF_2, gallic acid, phenylhydrazine hydrochloride,[31−33] and other antioxidants has been an effective way to inhibit Sn^{2+}. Recent reports suggested that Sn^{2+} is thermodynamically stable in acidic conditions.[34] However, only a few researchers have considered the role of multifunctional acidic salt additives in the simultaneous regulation of Sn^{2+} oxidation and perovskite crystallization.

Herein, we introduce a multifunctional acidic salt of dopamine hydrochloride (DACl) as a co-additive to synergistically modulate perovskite crystallization and Sn^{2+} oxidation for high-quality Sn perovskite films. The undissociated DACl in the solution facilitates the precipitation of the Sn perovskite, preferentially creating a pre-nucleation site to reduce the energy barrier, thereby inducing rapid nucleation before crystal growth. Meanwhile, the phenol group in DACl serves as an O_2 scavenger to inhibit Sn^{2+} oxidation and promote charge transport owing to the π-conjugation structure. The amino group and Cl^- ion bind to perovskite lattices for reduced defects. Moreover, the introduction of DACl provides a weakly acidic environment for enhanced thermodynamic stability of Sn^{2+}. The DACl-derived TPSCs realize a champion PCE reaching up to 11%, with an open-circuit voltage (V_{oc}) of 0.73 V. Meanwhile, the unencapsulated PSC shows long-term stability in full-sun illumination or air conditions.

RESULTS AND DISCUSSION

Tin perovskite film fabrication by spin-coated solution engineering usually creates a large number of defects and generates uncoordinated elements in the lattice. The schematic illustration of the modulation of perovskite defects and Sn^{2+} oxidation by the DACl additive is shown in Figure 1a. The Lewis base group (amine cation and chloride ion) in the DACl molecule coordinates with the uncoordinated Sn^{2+} of perovskite films to generate high-quality films with low defects. The reducing phenol group defers the Sn^{2+} oxidation in perovskite

https://doi.org/10.1021/acsami.2c11472
ACS Appl. Mater. Interfaces 2022, 14, 46801−46808

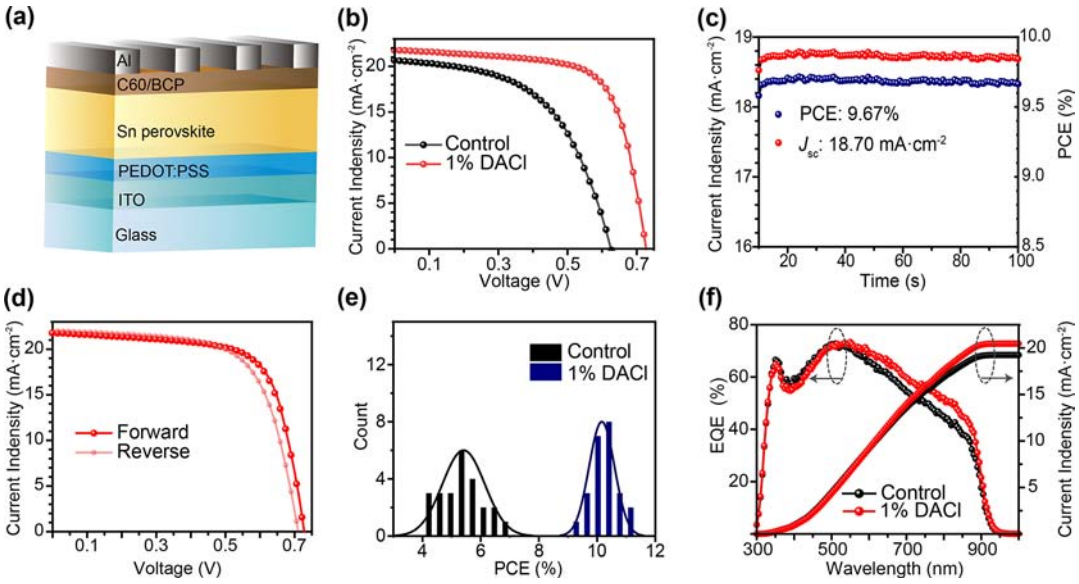

Figure 2. (a) Schematic diagram of the inverted PSCs. (b) $J-V$ curves of the control and DACl-derived device under 100 mW cm^{-2} AM 1.5G illumination. (c) Steady-state PCE and photocurrent at a constant bias of 0.52 V for the DACl-containing champion PSC. (d) $J-V$ curves of the DACl-derived PSC under reverse and forward scans. (e) PCE histograms measured for 24 devices. (f). EQE spectra of PSCs without and with 1% DACl additive.

precursor solution and films. When Sn perovskite films are exposed to aerobic conditions, −OH groups can transform into quinone's derivatives by providing electrons and hydrogen atoms (Figure 1a), thus continuously providing efficient protection to the Sn perovskite against oxidation.

The perovskite films are fabricated by the spin-coated method by introducing DACl (1.0 and 3.0 mol %) to the perovskite precursor solution. X-ray diffraction (XRD) analysis is performed to study the effect of DACl on perovskite crystallization, as shown in Figure 1b. The 1 mol % DACl-derived perovskite film shows much stronger diffraction peaks of perovskite crystals compared with pristine films at 14.0 and 28° indexed to (100) and (200) crystal planes, respectively, demonstrating that these crystals preferentially grow with improved crystallinity. When the concentration of DACl increases to 3 mol %, the diffraction peak of (h00) planes declines, owing to faster nucleation with a smaller crystal size. The DACl-derived (3 mol %) perovskite demonstrates a larger full width at half maximum (fwhm) of the (100) diffraction peak compared to 1 mol % DACl doping, further revealing the formation of a smaller size crystallite (Figure S1).

Scanning electron microscopy (SEM) images of perovskite films based on different concentrations of DACl are compared to further investigate the effects of DACl on the surface of Sn perovskite films (Figure 1c−e). The pristine film shows pinholes at grain boundaries and wrinkles on the grain surface. The grain size gradually decreases as a function of DACl concentrations. Since the solubility of DACl in the DMF and DMSO mixed solvent is low (~0.2 mg/mL), the Sn perovskite dissolves better in the mixed solution. The photographs of the Sn-based perovskite precursor with or without the DACl additive were recorded to visually observe the decrease of the supersaturation in the precursor (Figure S2). When the precursor solution (4 mol/L, 600 μL) was added with 5 mg of DACl, black perovskite crystals appeared in the precursor immediately, indicating that DACl could contribute to reduced supersaturation for more nucleation sites. Thus, DACl accelerates the Sn perovskite nucleation, thereby decreasing the grain size. The morphology is further investigated by atomic force microscopy (AFM) in a scanning area of 3.5 × 3.5 μm^2, as shown in Figure S3. The perovskite film without or with 1 mol % DACl additive shows root mean square values of 26.3 and 18.3 nm, respectively, indicating that the DACl significantly influences the surface roughness for reduced leakage current. These film characterizations suggest that DACl plays a crucial role in regulating the crystallization of high-quality perovskite films.

Based on these findings, inverted TPSCs with an ITO/PEDOT: PSS/$FA_{0.75}MA_{0.25}SnI_3$/C_{60}/BCP/Al structure are fabricated (Figures 2a and S4). The characteristic current density−voltage ($J-V$) curves are shown in Figure 2b and Table S1. The control TPSCs without the DACl additive display a champion PCE of 6.89% at a forward scan. Excitingly, the optimized device based on 1 mol % DACl achieves a much higher PCE of 10.93%, accompanied by significantly enlarged V_{oc} and FF of 0.73 V and 0.69, respectively. It can be found that the PCE of the device gradually decreases as the doping concentration increases from 1 to 5% (Table S1). The increased V_{oc} from 0.62 to 0.73 V and FF from 0.53 to 0.69 is due to the improved morphology of films and the reduced nonradiative recombination at trap states. In addition, DACl inhibits Sn^{2+} oxidation and promotes charge transport due to the improvement of crystal quality of perovskite films and the π-conjugation structure of DACl to reduce the V_{oc} loss (Figure 4d). Furthermore, the optimized device has a stable output PCE of 9.67% at the maximum power point under continuous sunlight with a stabilized J_{sc} of 18.70 mA·cm^{-2} (Figure 2c). The DACl-derived TPSC shows negligible hysteresis under forward and reverse scans (Figures 2d and S5). The hysteresis index [$PCE_{reverse}$ − $PCE_{forward}$/$PCE_{reverse}$] is also calculated as 0.06, which is lower than that of the control device (0.14). The reduced hysteresis behavior may be associated with the improved morphology of perovskite films and chemical interactions between DACl and perovskite structures, thus inhibiting the ions' migration. The parameter distribution with 24 different devices confirms that appropriate DACl content

https://doi.org/10.1021/acsami.2c11472
ACS Appl. Mater. Interfaces 2022, 14, 46801−46808

boosts device performance and improves reproducibility (Figures 2e and S6). The statistical measurements of 24 individual devices further confirm these results. The average PCE of TPSCs based on DACl is 10.16%, which is much higher than that of control devices (5.41%). Moreover, the integrated J_{sc} from the external quantum efficiency (EQE) for control and DACl-derived films also matches well with the calculated J_{sc} from $J-V$ curves (Figure 2f). SnF_2 may cause phase separation and crystallize and precipitate at the surface and grain boundaries of the perovskite film.[5] Therefore, the two additives could not only further protect the inner perovskite but also optimize the crystalline growth of the perovskite and reduce the possible phase separation effects caused by SnF_2. We also studied the effects of DACl and SnF_2 concentrations in the precursor on the device performance (Table S1 and Figure S7). It can be found that 10% SnF_2 and 1% DACl are the optimal conditions for the performance of TPSCs.

Stability is still a big obstacle in TPSC improvement; thus, the corresponding stability of devices is further investigated under varying conditions (light and air). When the photostability of TPSCs is measured under full-sun illumination in an N_2-filled glovebox, the normalized PCE of the DACl-derived device barely decreases after 150 h of aging (Figure 3a), while a serious decrease is observed in the control device with 10% left under the same condition. More importantly, the DACl-derived device maintains over 80% of its original PCE for 600 h, while the control device loses almost 100% of its PCE. The degradation in both normalized J_{sc} and FF of the TPSC based on DACl is also much slower than that of the control device (Figure 3b–d). Meanwhile, the stability of unencapsulated TPSCs is also tested in the air with RH ≈ 60% (Figure S8). Results reveal that the perovskite films without DACl show an obvious degradation and transparency after 24 h of exposure to humid air, whereas the DACl-derived perovskite films remain black. The unencapsulated DACl-derived device maintains ~60% of the initial PCE after 100 min of exposure, while the PCE of the control device decreases to ~5% at the same time. This improved air stability is further confirmed by XRD (Figure S8c,d). The good light and air stabilities indicate a low trap-state density and preferential growth of perovskite crystals by synergistically modulating perovskite crystallization and Sn^{2+} oxidation, resulting in high-quality tin perovskite films. Chemical interactions between DACl and Sn perovskites and the acidic environment are the primary reasons for improved stability.

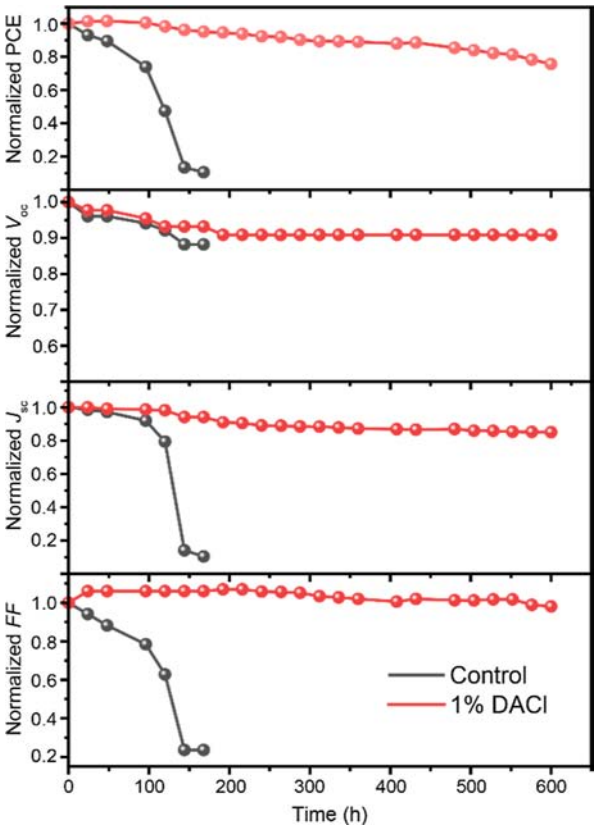

Figure 3. Device stability without encapsulating under combined full-spectrum light in the nitrogen atmosphere: normalized PCE, V_{oc}, J_{sc}, and FF evolution of the control and DACl-derived TPSCs.

To further explore the improved performance of the DACl additive-containing device, the corresponding optoelectrical properties of perovskite films are investigated. The perovskite film based on the DACl additive shows a much stronger steady-state photoluminescence (PL) emission peak than that of the control sample in the PL spectra (Figure 4a), indicating its higher crystal quality with reduced trap density for suppressed defect-induced nonradiative recombination. The presence of phase separation can be determined by the peak positions of the steady-state PL spectra (Figure S9).[35] The peak position of the PL spectrum for DACl-derived perovskite film is the same as that of control films, indicating that 1% DACl should not lead to phase separation. However, the peak position shows a significant blue-shift for the perovskite films with 5% DACl, leading to phase separation of the perovskite film. The average charge carrier lifetime (τ_{avg}) of DACl-derived perovskite films fitted by PL decay curves is remarkably prolonged from 2.21 to 4.82 ns (Figure 4b and Table S2). The fast decay lifetime τ_1 is due to the charge defect, and the slow τ_2 is attributed to the bimolecular radiative recombination.[36] With 1 mol % DACl doping, the proportion of τ_1 significantly reduces from 44.64 to 33.97%, indicating that the internal defect density decreases, while the percentage of τ_2 increases from 55.36 to 66.03% and the carrier lifetime increases from 3.15 to 6.11 ns, indicating that the charge carrier recombination is suppressed. These data also match well with PL spectra (Figure 4a). Incidentally, the photo-absorption of the perovskite film based on DACl shows slight enhancement compared to the control perovskite (Figure S10), suggesting the optimized light-harvesting capacity for enhancement J_{sc} in TPSCs. Moreover, light-intensity-dependent V_{oc} curves are measured to evaluate charge recombination losses (Figure 4c). V_{oc} is determined by the equation[37]

$$V_{oc} = \frac{n_{id}kT}{q}\ln\left(\frac{J_{ph}}{J_0} + 1\right) \quad (1)$$

where n_{id} is the ideality factor related to charge carrier recombination, and J_0 and J_{ph} are the saturated current density and photocurrent density, respectively. Compared to the control device, the DACl-derived TPSC shows a decrease in n_{id} from 1.68 to 1.38. The smaller n_{id} further indicates lower charge recombination, leading to higher V_{oc} and PCE.

The electrochemical impedance spectra (EIS, bias of 0.6 V) are used to further analyze the charge recombination and transport (Figure S11). The Nyquist plots of the control and

https://doi.org/10.1021/acsami.2c11472
ACS Appl. Mater. Interfaces 2022, 14, 46801−46808

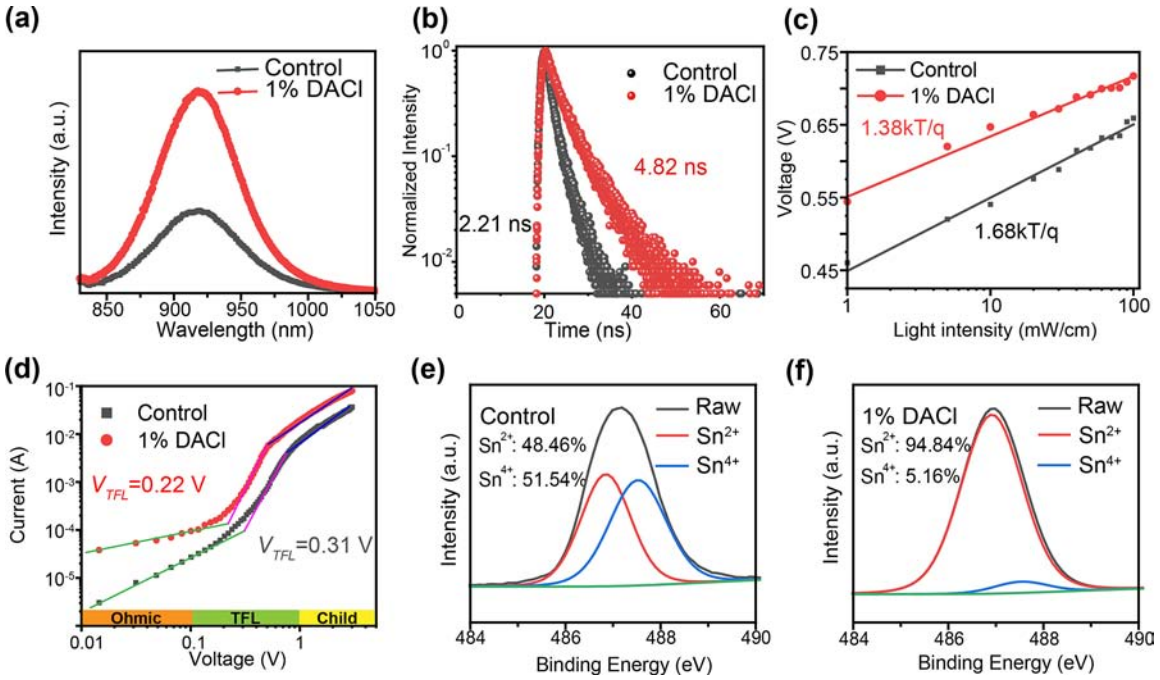

Figure 4. (a) Steady PL spectra, (b) time-resolved PL spectra, (c) light intensity-dependent V_{oc}, (d) hole-only devices to calculate the trap-state density, and (e–f) Sn $3d_{5/2}$ XPS of the control (e) and DACl-derived perovskite films (f).

DACl-derived TPSCs display the main arc related to the charge recombination resistance values (R_{rec}). The R_{rec} of the DACl-based device at 0.6 V is almost 15% higher than that of the control TPSC, revealing that the DACl-derived perovskite has a higher charge transfer rate and a lower recombination rate.

To further determine the trap-state density, space charge-limited current (SCLC) analysis is used for a device with ITO/PEDOT: PSS/$FA_{0.75}MA_{0.25}SnI_3$/MoO_3/Al structure (Figure S12). Dark J–V curves contain three typical regions—the ohmic region (n = 1) at a low voltage and the child region (n = 2) and the trap-filled limit (TFL) region (n > 3) at a high voltage (Figure 4d). The trap-state density (n_{trap}) was calculated by the equation[38]

$$n_{trap} = \frac{2\varepsilon\varepsilon_0 V_{TFL}}{qL^2} \quad (2)$$

where ε is the vacuum permittivity, ε_0 indicates the relative dielectric constant, L is the thickness of the film, and V_{TFL} represents the trap filling limited voltages. The V_{TFL} of control and DACl-derived perovskite films is 0.31 and 0.22 V, respectively. The hole trap-state densities are 4.97×10^{16} and 3.52×10^{16} cm^{-3}, respectively, indicating an effective reduction in defects. These results further confirm that DACl addition can suppress ion migration and hysteresis behaviors by improving the quality of the perovskite crystal. Also, hole mobility can be achieved from the SCLC model of the child region by the following equation[39]

$$J = \frac{9}{8}\varepsilon_0\varepsilon_r\mu\frac{V^2}{L^3} \quad (3)$$

The hole mobility for the DACl-derived perovskite (2.58×10^{-5} cm^2 V^{-1} s^{-1}) is higher than that of the control sample (8.40×10^{-6} cm^2 V^{-1} s^{-1}), suggesting that the DACl-derived perovskite is more favorable to charge transport. The conductivity of the DACl-derived perovskite film reaches 1.51×10^{-2} mS·cm^{-1} (Figure S13), which is much higher than that of the control perovskite film (8.79×10^{-3} mS·cm^{-1}). The enhancement of conductivity and hole mobility should depend largely on the improvement of crystal quality, and the π-conjugation structure also has an influence on the enhancement of hole mobility and conductivity. Furthermore, almost 2 orders of lower leakage current have been shown in DACl-derived devices compared to the control TPSC (Figure S14). The higher leakage is related to the higher p-type doping of the perovskite due to Sn^{2+} oxidization. Thus, the reduced leakage current also indicates a significantly decreased background carrier density.

Sn^{2+} shows better stability in acidic solutions due to the reduced reduction potential in acidic environments.[40] The pH test shows the lower pH of the precursor doped with DACl (~6.0) than the control group (~7.0), suggesting that DACl does create a weakly acidic environment that may inhibit Sn^{2+} oxidation. To demonstrate better inhibition of Sn^{2+} oxidation in DACl-containing perovskite films, the Sn^{2+} and Sn^{4+} contents are investigated by X-ray photoelectron spectroscopy (XPS). The XPS peak of Sn fitted by a Gaussian function is split into Sn^{2+} and Sn^{4+} states (Figure 4e,f). The Sn^{4+} content of 1 mol % DACl remarkably decreases to 5.16%, which is much lower than that of the pristine (51.54%), indicating that the DACl additive significantly inhibits the generation of Sn^{4+} and improves the stability of TPSCs.

The XPS spectra also confirm that the Sn from $FA_{0.75}MA_{0.25}SnI_3$ is the reaction site for coordination to the DACl molecule as the peak binding energy of the Sn $3d_{5/2}$ spectrum exhibits an obvious movement toward lower binding energy (~0.3 eV) from the control to the DACl-derived film (Figure 4e,f). Fourier transform infrared (FTIR) spectra are also utilized to further investigate the chemical bond between DACl and perovskites (Figure S15a). The N–H bending vibration for the DACl molecule is located at 1753 cm^{-1}, which shifts to 1719 cm^{-1} in the $FA_{0.75}MA_{0.25}SnI_3$-DACl

https://doi.org/10.1021/acsami.2c11472
ACS Appl. Mater. Interfaces 2022, 14, 46801–46808

sample,[41] demonstrating the coordination between the N−H unit and perovskite. The reducing hydroxyl groups (-OH) can be effectively transferred to quinone groups in air, which could be further verified by FTIR (Figure S15b). It can be found that the carbonyl stretching vibration peak exists at around 1633 cm^{-1}, which should result in quinone group generation.[33]

CONCLUSIONS

In summary, dual regulation of crystallization and Sn^{2+} oxidation achieved by introducing DACl as a co-additive with SnF_2 into the perovskite precursor solution illustrates an efficient strategy for improving the device performance. The undissociated DACl reduces the supersaturated concentration of the Sn perovskite precursor by preferentially creating pre-nucleation sites for fast nucleation before crystal growth. The reductive phenol groups in DACl inhibit Sn^{2+} oxidation and promote charge transport via a π-conjugated structure. The amino group and Cl^- ion are bound to perovskite lattices (iodide ion vacancies and uncoordinated Sn^{2+}) to reduce defects. As a result, the $FA_{0.75}MA_{0.25}SnI_3$ device containing 1 mol % DACl generates a maximum PCE approaching 11%, with significantly improved FF from 53.2 to 68.9%. Moreover, the unencapsulated device shows much better stability in full-sun illumination or air conditions. For continuous full-sun illumination, the DACl-derived device shows less than 20% decay in initial PCE after 600 h. This work can provide a new possible direction to screen out multifunctional additives in Sn perovskite film preparation and provide a guideline for constructing high-performance lead-free photovoltaic devices.

EXPERIMENTAL SECTION

Device Fabrication. Perovskite solar cells were fabricated with an inverted structure of ITO/PEDOT:PSS/perovskite/C_{60}/BCP/Al. PEDOT:PSS was spin-coated on clean ITO glass at 4500 rpm for 45 s and then annealed at 120 °C for 25 min. The PEDOT:PSS-resolved ITO was then delivered to a glovebox full of N_2. The Sn perovskite precursor was composed of 1.0 mol/L SnI_2, 0.75 mol/L FAI, 0.25 mol/L MAI, and 0.1 mol/L SnF_2, dissolved in the mixed solvent of DMF/DMSO (4/1, v/v), and stirred at 25 °C for 1 h. For the DACl-contained precursor, the molar ratios of DACl and SnI_2 were 1, 3, and 5%, respectively. The $FA_{0.75}MA_{0.25}SnI_3$ precursor was then dripped onto the ITO/PEDOT:PSS surface and spin-coated at 5000 rpm for 36 s; and 160 μL of chlorobenzene was dripped onto the perovskite at the 13th s of the spin-coating step to produce a dense film of the perovskite crystal; the film was then thermally annealed at 75 °C for 10 min, ultimately evaporating C_{60} (25 nm), BCP (6 nm), and Al electrode (100 nm) layers sequentially. The active area of a single device was determined by a mask with 0.09 cm^2 perforation.

ASSOCIATED CONTENT

Supporting Information

The Supporting Information is available free of charge at https://pubs.acs.org/doi/10.1021/acsami.2c11472.

Materials; characterization; fwhm and AFM images of the perovskite films; photographs of the perovskite precursor solutions; energy-level diagram of the inverted TPSCs; $J-V$ curves of the control device under different scans; device performance statistics on V_{oc} and FF of the control and DACl-derived PSCs; $J-V$ curves of the devices by varying the SnF_2 and DACl concentrations; stability characterization of the perovskite films and devices in humidity conditions; PL spectra of the perovskite film with different concentration of DACl; absorption spectra of the perovskite films; Nyquist plots of the EIS measurements and dark-current characteristics of control and DACl-derived TPSCs under dark conditions; schematic structure of the hole-only device for calculation of the hole mobility and trap density; conductivity and FTIR spectra of the perovskite with and without DACl; table of the device performance parameters of the TPSCs based on varied the DACl concentrations; and table of TRPL curve-fitted parameters (PDF)

AUTHOR INFORMATION

Corresponding Authors

Runfeng Chen − *Key Laboratory for Organic Electronics and Information Displays (KLOEID) & Jiangsu Key Laboratory for Biosensors, Institute of Advanced Materials (IAM), Jiangsu National Synergetic Innovation Center for Advanced Materials (SICAM), Nanjing University of Posts & Telecommunications, Nanjing 210023, China;* orcid.org/0000-0003-0222-0296; Email: iamrfchen@njupt.edu.cn

Ligang Xu − *Key Laboratory for Organic Electronics and Information Displays (KLOEID) & Jiangsu Key Laboratory for Biosensors, Institute of Advanced Materials (IAM), Jiangsu National Synergetic Innovation Center for Advanced Materials (SICAM), Nanjing University of Posts & Telecommunications, Nanjing 210023, China; Wuhan National Laboratory for Optoelectronics, Huazhong University of Science and Technology, Wuhan, Hubei 430074, China;* orcid.org/0000-0002-9414-0674; Email: iamlgxu@njupt.edu.cn

Authors

Wenbo Jia − *Key Laboratory for Organic Electronics and Information Displays (KLOEID) & Jiangsu Key Laboratory for Biosensors, Institute of Advanced Materials (IAM), Jiangsu National Synergetic Innovation Center for Advanced Materials (SICAM), Nanjing University of Posts & Telecommunications, Nanjing 210023, China*

Zijie Wei − *Key Laboratory for Organic Electronics and Information Displays (KLOEID) & Jiangsu Key Laboratory for Biosensors, Institute of Advanced Materials (IAM), Jiangsu National Synergetic Innovation Center for Advanced Materials (SICAM), Nanjing University of Posts & Telecommunications, Nanjing 210023, China*

Bingxu Liu − *Key Laboratory for Organic Electronics and Information Displays (KLOEID) & Jiangsu Key Laboratory for Biosensors, Institute of Advanced Materials (IAM), Jiangsu National Synergetic Innovation Center for Advanced Materials (SICAM), Nanjing University of Posts & Telecommunications, Nanjing 210023, China*

Dongdong Yan − *Key Laboratory for Organic Electronics and Information Displays (KLOEID) & Jiangsu Key Laboratory for Biosensors, Institute of Advanced Materials (IAM), Jiangsu National Synergetic Innovation Center for Advanced Materials (SICAM), Nanjing University of Posts & Telecommunications, Nanjing 210023, China*

Yunze Huang − *Key Laboratory for Organic Electronics and Information Displays (KLOEID) & Jiangsu Key Laboratory for Biosensors, Institute of Advanced Materials (IAM), Jiangsu National Synergetic Innovation Center for Advanced Materials (SICAM), Nanjing University of Posts & Telecommunications, Nanjing 210023, China*

Meicheng Li − *State Key Laboratory of Alternate Electrical Power System with Renewable Energy Sources, School of New Energy, North China Electric Power University, Beijing 102206, China;* orcid.org/0000-0002-0731-741X

Ye Tao − *Key Laboratory for Organic Electronics and Information Displays (KLOEID) & Jiangsu Key Laboratory for Biosensors, Institute of Advanced Materials (IAM), Jiangsu National Synergetic Innovation Center for Advanced Materials (SICAM), Nanjing University of Posts & Telecommunications, Nanjing 210023, China; State Key Laboratory of Alternate Electrical Power System with Renewable Energy Sources, School of New Energy, North China Electric Power University, Beijing 102206, China; Wuhan National Laboratory for Optoelectronics, Huazhong University of Science and Technology, Wuhan, Hubei 430074, China;* orcid.org/0000-0002-5080-2533

Complete contact information is available at: https://pubs.acs.org/10.1021/acsami.2c11472

Notes

The authors declare no competing financial interest.

■ ACKNOWLEDGMENTS

The authors thank the support from the National Natural Science Foundation of China (62274094, 61604079, 51972110, and 91833306), the Natural Science Foundation of Jiangsu Higher Education Institutions(22KJB510011), the State Key Laboratory of Alternate Electrical Power System with Renewable Energy Sources(Grant no. LAPS22006), the Open Project Program of Wuhan National Laboratory for Optoelectronics NO.2020WNLOKF012, Beijing Natural Science Foundation (2222076), and Huali Talents Program of Nanjing University of Posts and Telecommunications.

■ REFERENCES

(1) NREL. Best Research Cell Efficiencies Chart. https://www.nrel.gov/pv/assets/pdfs/best-research-cell-efficiencies-rev220630.pdf (accessed 2022-06-30).

(2) Kamarudin, M. A.; Hirotani, D.; Wang, Z.; Hamada, K.; Nishimura, K.; Shen, Q.; Toyoda, T.; Iikubo, S.; Minemoto, T.; Yoshino, K.; Hayase, S. Suppression of Charge Carrier Recombination in Lead-Free Tin Halide Perovskite Via Lewis Base Post-Treatment. *J. Phys. Chem. Lett.* **2019**, *10*, 5277−5283.

(3) Jiang, X.; Wang, F.; Wei, Q.; Li, H.; Shang, Y.; Zhou, W.; Wang, C.; Cheng, P.; Chen, Q.; Chen, L.; Ning, Z. Ultra-High Open-Circuit Voltage of Tin Perovskite Solar Cells Via an Electron Transporting Layer Design. *Nat. Commun.* **2020**, *11*, 1245.

(4) Wu, T.; Liu, X.; He, X.; Wang, Y.; Meng, X.; Noda, T.; Yang, X.; Han, L. Efficient and Stable Tin-Based Perovskite Solar Cells by Introducing π-conjugated Lewis Base. *Sci. China Chem.* **2020**, *63*, 107.

(5) Xu, L.; Feng, X.; Jia, W.; Lv, W.; Mei, A.; Zhou, Y.; Zhang, Q.; Chen, R.; Huang, W. Recent Advances and Challenges of Inverted Lead-Free Tin-Based Perovskite Solar Cells. *Energy Environ. Sci.* **2021**, *14*, 4292−4317.

(6) Chang, B.; Li, B.; Wang, Z.; Li, H.; Wang, L.; Pan, L.; Li, Z.; Yin, L. Efficient Bulk Defect Suppression Strategy in $FASnI_3$ Perovskite for Photovoltaic Performance Enhancement. *Adv. Funct. Mater.* **2022**, *32*, 2107710.

(7) Xu, L.; Zhang, C.; Feng, X.; Lv, W. X.; Huang, Z.; Lv, W.; Zheng, C.; Xing, G.; Huang, W.; Chen, R. Vapor Incubation of $FASnI_3$ Films for Efficient and Stable Lead-Free Inverted Perovskite Solar Cells. *J. Mater. Chem. A* **2021**, *9*, 16943−16951.

(8) Slavney, A. H.; Hu, T.; Lindenberg, A. M.; Karunadasa, H. I. A Bismuth-Halide Double Perovskite with Long Carrier Recombination Lifetime for Photovoltaic Applications. *J. Am. Chem. Soc.* **2016**, *138*, 2138−2141.

(9) Ghosh, B.; Chakraborty, S.; Wei, H.; Guet, C.; Li, S.; Mhaisalkar, S.; Mathews, N. Poor Photovoltaic Performance of $Cs_3Bi_2I_9$: an Insight through First-Principles Calculations. *J. Phys. Chem. C* **2017**, *121*, 17062−17067.

(10) Vargas, B.; Ramos, E.; Pérez-Gutiérrez, E.; Alonso, J. C.; Solis-Ibarra, D. A Direct Bandgap Copper-Antimony Halide Perovskite. *J. Am. Chem. Soc.* **2017**, *139*, 9116−9119.

(11) Xiao, Z.; Du, K.-Z.; Meng, W.; Wang, J.; Mitzi, D. B.; Yan, Y. Intrinsic Instability of Cs_2InMX_6 (M= Bi, Sb; X= Halogen) Double Perovskites: a Combined Density Functional Theory and Experimental Study. *J. Am. Chem. Soc.* **2017**, *139*, 6054−6057.

(12) Ray, D.; Clark, C.; Pham, H. Q.; Borycz, J.; Holmes, R. J.; Aydil, E. S.; Gagliardi, L. Computational Study of Structural and Electronic Properties of Lead-Free $CsMI_3$ Perovskites (M= Ge, Sn, Pb, Mg, Ca, Sr, and Ba). *J. Phys. Chem. C* **2018**, *122*, 7838−7848.

(13) Lu, J.; Guan, X.; Li, Y.; Lin, K.; Feng, W.; Zhao, Y.; Yan, C.; Li, M.; Shen, Y.; Qin, X.; Wei, Z. Dendritic $CsSnI_3$ for Efficient and Flexible Near-Infrared Perovskite Light-Emitting Diodes. *Adv. Mater.* **2021**, *33*, 2104414.

(14) Jiang, X.; Zang, Z.; Zhou, Y.; Li, H.; Wei, Q.; Ning, Z. Tin Halide Perovskite Solar Cells: an Emerging Thin-Film Photovoltaic Technology. *Acc. Mater. Res.* **2021**, *2*, 210−219.

(15) Ke, W.; Stoumpos, C. C.; Logsdon, J. L.; Wasielewski, M. R.; Yan, Y.; Fang, G.; Kanatzidis, M. G. TiO_2-ZnS Cascade Electron Transport Layer for Efficient Formamidinium Tin Iodide Perovskite Solar Cells. *J. Am. Chem. Soc.* **2016**, *138*, 14998−15003.

(16) Shih, C.-C.; Wu, C.-G. Synergistic Engineering of the Conductivity and Surface Properties of PEDOT:PSS-Based HTLs for Inverted Tin Perovskite Solar Cells to Achieve Efficiency over 10. *ACS Appl. Mater. Interfaces* **2022**, *14*, 16125−16135.

(17) Ye, T.; Wang, K.; Hou, Y.; Yang, D.; Smith, N.; Magill, B.; Yoon, J.; Mudiyanselage, R. R. H. H.; Khodaparast, G. A.; Wang, K.; Priya, S. Ambient-Air-Stable Lead-Free $CsSnI_3$ Solar Cells with Greater than 7.5% Efficiency. *J. Am. Chem. Soc.* **2021**, *143*, 4319−4328.

(18) Jokar, E.; Chien, C. H.; Tsai, C. M.; Fathi, A.; Diau, E. W. G. Robust Tin-Based Perovskite Solar Cells with Hybrid Organic Cations to Attain Efficiency Approaching 10. *Adv. Mater.* **2019**, *31*, No. e1804835.

(19) Cao, X.; Li, J.; Dong, H.; Li, P.; Fan, Q.; Xu, R.; Li, H.; Zhou, G.; Wu, Z. Stability Improvement of Tin-Based Halide Perovskite by Precursor-Solution Regulation with Dual-Functional Reagents. *Adv. Funct. Mater.* **2021**, *31*, 2104344.

(20) Fang, H.-H.; Adjokatse, S.; Shao, S.; Even, J.; Loi, M. A. Long-Lived Hot-Carrier Light Emission and Large Blue Shift in Formamidinium Tin Triiodide Perovskites. *Nat. Commun.* **2018**, *9*, 245.

(21) Song, T.-B.; Yokoyama, T.; Stoumpos, C. C.; Logsdon, J.; Cao, D. H.; Wasielewski, M. R.; Aramaki, S.; Kanatzidis, M. G. Importance of Reducing Vapor Atmosphere in the Fabrication of Tin-Based Perovskite Solar Cells. *J. Am. Chem. Soc.* **2017**, *139*, 836−842.

(22) Sanchez-Diaz, J.; Sánchez, R. S.; Masi, S.; Krecmarová, M.; Alvarez, A. O.; Barea, E. M.; Rodriguez-Romero, J.; Chirvony, V. S.; Sánchez-Royo, J. F.; Martinez-Pastor, J. P.; Mora-Seró, I. Tin Perovskite Solar Cells with >1,300 h of Operational Stability in N_2 through a Synergistic Chemical Engineering Approach. *Joule* **2022**, *6*, 861−883.

(23) Jiang, X.; Li, H.; Zhou, Q.; Wei, Q.; Wei, M.; Jiang, L.; Wang, Z.; Peng, Z.; Wang, F.; Zang, Z.; Xu, K.; Hou, Y.; Teale, S.; Zhou, W.; Si, R.; Gao, X.; Sargent, E. H.; Ning, Z. One-Step Synthesis of SnI_2·$(DMSO)_x$ Adducts for High-Performance Tin Perovskite Solar Cells. *J. Am. Chem. Soc.* **2021**, *143*, 10970−10976.

(24) Wang, F.; Jiang, X.; Chen, H.; Shang, Y.; Liu, H.; Wei, J.; Zhou, W.; He, H.; Liu, W.; Ning, Z. 2D-Quasi-2D-3D Hierarchy Structure for Tin Perovskite Solar Cells with Enhanced Efficiency and Stability. *Joule* **2018**, *2*, 2732−2743.

(25) Xu, L.; Qian, M.; Zhang, C.; Lv, W.; Jin, J.; Zhang, J.; Zheng, C.; Li, M.; Chen, R.; Huang, W. In Situ Construction of Gradient Heterojunction Using Organic VO_x Precursor for Efficient and Stable Inverted Perovskite Solar Cells. *Nano Energy* **2020**, *67*, 104244.
(26) Xu, L.; Liu, Y.; Qiu, W.; Li, Y.; Wang, H.; Li, M.; Xian, L.; Zheng, C.; Chen, Y.; Chen, R. Conjugated Molecule Doping of Triphenylamine-Based Hole-Transport Layer for High-Performance Perovskite Solar Cells. *J. Power Sources* **2021**, *506*, 230120.
(27) Xu, L.; Wang, H.; Feng, X.; Zhou, Y.; Chen, Y.; Chen, R.; Huang, W. Vanadium Oxide-Modified Triphenylamine-Based Hole-Transport Layer for Highly Reproducible and Efficient Inverted Perovskite Solar Cells. *Adv. Photonics Res.* **2021**, *2*, 2000132.
(28) Xu, L.; Wu, D.; Lv, W.; Xiang, Y.; Liu, Y.; Tao, Y.; Yin, J.; Qian, M.; Li, P.; Zhang, L.; Chen, S.; Mohammed, O. F.; Bakr, O. M.; Duan, Z.; Chen, R.; Huang, W. Resonance-Mediated Dynamic Modulation of Perovskite Crystallization for Efficient and Stable Solar Cells. *Adv. Mater.* **2022**, *34*, 2107111.
(29) Park, K.; Lee, J.-H.; Lee, J.-W. Surface Defect Engineering of Metal Halide Perovskites for Photovoltaic Applications. *ACS Energy Lett.* **2022**, *7*, 1230−1239.
(30) Leijtens, T.; Prasanna, R.; Gold-Parker, A.; Toney, M. F.; McGehee, M. D. Mechanism of Tin Oxidation and Stabilization by Lead Substitution in Tin Halide Perovskites. *ACS Energy Lett.* **2017**, *2*, 2159−2165.
(31) Gu, F.; Ye, S.; Zhao, Z.; Rao, H.; Liu, Z.; Bian, Z.; Huang, C. Improving Performance of Lead-Free Formamidinium Tin Triiodide Perovskite Solar Cells by Tin Source Purification. *Sol. RRL* **2018**, *2*, 1800136.
(32) Wang, C.; Gu, F.; Zhao, Z.; Rao, H.; Qiu, Y.; Cai, Z.; Zhan, G.; Li, X.; Sun, B.; Yu, X. Self-Repairing Tin-Based Perovskite Solar Cells with a Breakthrough Efficiency over 11%. *Adv. Mater.* **2020**, *32*, 1907623.
(33) Wang, T.; Tai, Q.; Guo, X.; Cao, J.; Liu, C.-K.; Wang, N.; Shen, D.; Zhu, Y.; Lee, C.-S.; Yan, F. Highly Air-Stable Tin-Based Perovskite Solar Cells through Grain-Surface Protection by Gallic Acid. *ACS Energy Lett.* **2020**, *5*, 1741−1749.
(34) Su, Y.; Yang, J.; Liu, G.; Sheng, W.; Zhang, J.; Zhong, Y.; Tan, L.; Chen, Y. Acetic Acid-Assisted Synergistic Modulation of Crystallization Kinetics and Inhibition of Sn^{2+} Oxidation in Tin-Based Perovskite Solar Cells. *Adv. Funct. Mater.* **2022**, *32*, 2109631.
(35) Tao, J.; Liu, X.; Shen, J.; Han, S.; Guan, L.; Fu, G.; Kuang, D.; Yang, S. F-Type Pseudo-Halide Anions for High-Efficiency and Stable Wide-Band-Gap Inverted Perovskite Solar Cells with Fill Factor Exceeding 84%. *ACS Nano* **2022**, *16*, 10798−10810.
(36) Li, B.; Di, H.; Chang, B.; Yin, R.; Fu, L.; Zhang, Y. N.; Yin, L. Efficient Passivation Strategy on Sn Related Defects for High Performance All-Inorganic $CsSnI_3$ Perovskite Solar Cells. *Adv. Funct. Mater.* **2021**, *31*, 2007447.
(37) Wan, Z.; Ren, S.; Lai, H.; Jiang, Y.; Wu, X.; Luo, J.; Wang, Y.; He, R.; Chen, Q.; Hao, X.; Wang, Y.; Wu, L.; Constantinou, I.; Zhang, W. H.; Zhang, J.; Zhao, D. Suppression of Nonradiative Recombination by Vacuum-Assisted Process for Efficient Lead-Free Tin Perovskite Solar Cells. *Adv. Mater. Interfaces* **2021**, *8*, 2100135.
(38) Lee, L.; Baek, J.; Park, K. S.; Lee, Y. E.; Shrestha, N. K.; Sung, M. M. Wafer-Scale Single-Crystal Perovskite Patterned Thin Films Based on Geometrically-Confined Lateral Crystal Growth. *Nat. Commun.* **2017**, *8*, 15882.
(39) Song, Y.; Bi, W.; Wang, A.; Liu, X.; Kang, Y.; Dong, Q. Efficient Lateral-Structure Perovskite Single Crystal Solar Cells with High Operational Stability. *Nat. Commun.* **2020**, *11*, 274.
(40) Abdel-Shakour, M.; Chowdhury, T. H.; Matsuishi, K.; Bedja, I.; Moritomo, Y.; Islam, A. High-Efficiency Tin Halide Perovskite Solar Cells: The Chemistry of Tin (II) Compounds and Their Interaction with Lewis Base Additives during Perovskite Film Formation. *Sol. RRL* **2021**, *5*, 2000606.
(41) Ye, T.; Wang, X.; Wang, K.; Ma, S.; Yang, D.; Hou, Y.; Yoon, J.; Wang, K.; Priya, S. Localized Electron Density Engineering for Stabilized B-γ $CsSnI_3$-Based Perovskite Solar Cells with Efficiencies> 10%. *ACS Energy Lett.* **2021**, *6*, 1480−1489.

https://doi.org/10.1021/acsami.2c11472
ACS Appl. Mater. Interfaces 2022, 14, 46801−46808